Journal of Non-Newtonian Fluid Mechanics, 9 (1981) 269–300
Elsevier Scientific Publishing Company, Amsterdam—Printed in The Netherlands

RIMMING FLOW OF A VISCOELASTIC LIQUID INSIDE A ROTATING HORIZONTAL CYLINDER

J. SANDERS, D.D. JOSEPH AND G.S. BEAVERS

Department of Aerospace Engineering and Mechanics, University of Minnesota, Minneapolis, Minnesota 55455 (U.S.A.)

(Received June 19, 1981)

Summary

The flow of a simple liquid coating the inside of a horizontal, steadily rotating cylinder is investigated. The theory, in combination with the experiments, allows us to determine the complex viscosity $\eta^*(\Omega)$ of the liquid, characterizing its viscoelastic properties.

In the theory, rigid rotation of the flow in the absence of gravity is perturbed with small gravity. This includes the perturbation of the free surface as well as the stress. The representation of the functional derivation of the stress by integrals is assumed. No restriction on the fluid memory is made.

In the experiment, a continuous trace of the liquid film thickness as a function of the angle is produced. The liquid film thickness is measured by light absorption. The complex viscosity $\eta^*(\Omega)$ obtained from the free surface shape and the theory is compared with the corresponding result from measurements on an oscillating cone-and-plate rheometer for two viscoelastic polymer solutions (TLA 227 and STP).

Some qualitative experimental results on the stability phenomena are presented showing the formation of liquid cells when the cylinder is rotating slowly.

1. Introduction

Rimming flow is the flow of a liquid layer around the inside surface of a rotating horizontal drum or cylinder. Rimming flows occur in a variety of industrial applications in which a layer of viscous liquid is required to be

0377-0257/81/0000–0000/$02.75

spread on a solid surface. Some examples given by Ruschak and Scriven [1] are "... in cream separators, in liquid degassers, in some coating operations for pipes and tubes, in rotational moulding and spin casting of plastics, in the casting of molten metal or cement into pipes and columns, and even in the drying of fine powder in a rotating oven." In this paper we develop a perturbation solution for the rimming flow of a viscoelastic liquid, and we show how the solution leads to a simple, practical method for the measurement of the complex viscosity of the liquid.

The problem we consider is that of a large, horizontal, hollow cylinder rotating steadily around its axis. The inside of the cylinder is coated with a viscoelastic liquid. In the absence of gravity, the liquid will rotate rigidly and coat the cylinder with a film of constant thickness. Perturbing the problem with "small" gravity will therefore perturb the motion, the stress and the location of the free surface.

We shall assume that the viscoelastic liquid is an incompressible simple fluid; that is, a fluid whose stress depends on the history of the right relative Cauchy Green tensor $\boldsymbol{C}_t(\tau)$ [2].

Joseph [3] derived perturbation equations for motions of a simple fluid perturbing rigid motions under the assumption that the Fréchet derivatives of the stress on the zero history can be represented by integrals with kernel functions of the fading memory type. In this study we combine the theory of rotating simple fluids with techniques for studying perturbations of the domain occupied by the fluid [4] to determine the dependence of film thickness variation and other properties of rimming flow on rheological parameters. Since our analysis is carried out only to first order, the problem is linear viscoelastic and it depends on the material only through the complex viscosity. Our solution of this problem reduces to the one solved by Ruschak and Scriven [1], when the fluid is Newtonian.

Numerical studies of rimming flows of Newtonian fluids, which are not restricted to perturbations, have been given by Orr and Scriven [5] and by Deiber and Cerro [6]. In the non-Newtonian case, general constitutive equations are known only in the sense of perturbations. Global numerical results are possible only under some more-or-less arbitrary assumption that the constitutive equation of the fluid is described by some particular model.

2. Formulation

In this section we derive the equations governing rimming flow and the stability of rimming flow. The fluid is in an annular-like region

$$\mathcal{V}(t) = \{r,\phi | R(\phi,t) \leq r \leq R_0, \quad 0 \leq \phi < 2\pi\}$$

between a solid cylinder whose constant angular velocity at $r = R_0$ is Ω, and

a fluid–air interface at $r = R(\phi, t)$ (see Fig. 1).

The equations of motion for a simple, incompressible fluid in the configuration shown in Fig. 1 are

$$\rho\left(\frac{\partial \boldsymbol{V}}{\partial t} + (\boldsymbol{V}\cdot\nabla)\boldsymbol{V}\right) = \nabla\Phi + \nabla\cdot\boldsymbol{S}, \quad \nabla\cdot\boldsymbol{V} = 0 \qquad \text{in } \mathcal{V}(t), \tag{2.1}$$

where the head Φ is given by

$$\Phi = -p + p_a - \rho g y = -p + p_a - \rho g r \sin\phi. \tag{2.2}$$

p_a is the pressure of the atmosphere, and $\boldsymbol{S}$ is the extra stress given by

$$\boldsymbol{S} = \mathop{\mathcal{F}}_{s=0}^{\infty}[\boldsymbol{G}(s)],$$

where $\mathcal{F}[\ ]$ is a functional at a particle (presently at $\boldsymbol{x}$) of the history $\boldsymbol{G}(s) = \boldsymbol{F}_t^{\mathrm{T}}(t-s)\boldsymbol{F}_t(t-s) - \boldsymbol{1}$ of the deformation. The relative deformation gradient is $\boldsymbol{F}_t(t-s)$ where

$$\boldsymbol{F}_t(t-s) \equiv \nabla\boldsymbol{\chi}_t(\boldsymbol{x}, t-s),$$

and $\boldsymbol{\chi}_t(\boldsymbol{x}, t-s)$ is the backward path line of a particle which at the present time t is at $\boldsymbol{\chi}_t(\boldsymbol{x}, t) = \boldsymbol{x}$. The velocity is $\boldsymbol{V}(\boldsymbol{x}, t)$, ρ is the density of the fluid, p is the pressure and g is the acceleration of gravity.

The liquid adheres to the inside surface of the solid cylinder,

$$\boldsymbol{V}(R_0, \phi, t) = \Omega R_0 \boldsymbol{e}_\phi.$$

We consider two-dimensional motions and only these. Then at the free surface

$$F(r, \phi, t) = r - R(\phi, t) = 0 \tag{2.3}$$

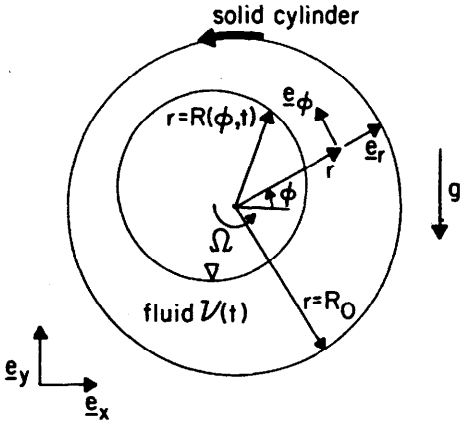

Fig. 1. Rimming flow.

we have

$$u = \frac{\partial R}{\partial t} + \frac{v}{r}\frac{\partial R}{\partial \phi}, \tag{2.4}$$

where $V=(u,v)$ in cylindrical coordinates (r,ϕ). At the free surface $r = R(\phi,t)$, the stresses are balanced by the surface tension force with surface tension σ and curvature χ:

$$(p-p_a)\boldsymbol{n} - \boldsymbol{S}\cdot\boldsymbol{n} + \sigma\chi\boldsymbol{n} = 0,$$

$$\chi = \frac{R^2 + 2R_\phi^2 - RR_{\phi\phi}}{\left(R^2+R_\phi^2\right)^{3/2}}, \tag{2.5}$$

where $\boldsymbol{n}$ is the normal to the free surface and

$$p - p_a = -\Phi - \rho g R(\phi,t)\sin\phi. \tag{2.6}$$

We now project (2.5) with $\boldsymbol{n}$, and $\boldsymbol{t}$ perpendicular to $\boldsymbol{n}$, to express the balance of normal stresses and shear stresses on the free surface $r = R(\phi,t)$. Thus,

$$p - p_a - \frac{1}{R^2+R_\phi^2}\left(R^2 S\langle rr\rangle - 2RR_\phi S\langle r\phi\rangle + R_\phi^2 S\langle\phi\phi\rangle\right) + \sigma\chi = 0, \tag{2.7}$$

and

$$RR_\phi S\langle rr\rangle + \left(R^2 - R_\phi^2\right)S\langle r\phi\rangle - RR_\phi S\langle\phi\phi\rangle = 0, \tag{2.8}$$

where subscripts denote partial derivatives and angle brackets denote components in (r,ϕ). Using (2.6) and (2.8) we may rewrite (2.7) as

$$R(-\Phi - \rho g R\sin\phi) + \left(R_\phi S\langle r\phi\rangle - RS\langle rr\rangle\right) + \sigma R\chi = 0. \tag{2.9}$$

Finally, we prescribe the amount of liquid coating the cylinder per unit length by prescribing its area in terms of an average film thickness D. Thus

$$(R_0 - D)^2 = \frac{1}{2\pi}\int_0^{2\pi} R^2(\phi,t)\,\mathrm{d}\phi. \tag{2.10}$$

We eliminate $\nabla\cdot V = 0$ by introducing a stream function $\psi(r,\phi,t)$ such that

$$(u,v) = \left(\frac{1}{r}\psi_\phi, -\psi_r\right). \tag{2.11}$$

We must solve

$$\rho\left(\frac{\partial V}{\partial t} + (V\cdot\nabla)V\right) = \nabla\Phi + \operatorname{div}\boldsymbol{S}, \tag{2.12}$$

where $V=(u,v)$ is given by (2.11); and at the cylinder surface

$$\psi(R_0,\phi,t) = \psi_r(R_0,\phi,t) + \Omega R_0 = 0. \tag{2.13}$$

At the free surface $r = R(\phi,t)$:

$$\psi_\phi + R_\phi \psi_r = RR_t, \tag{2.14}$$

$$RR_\phi(S\langle rr\rangle - S\langle\phi\phi\rangle) + \left(R^2 - R_\phi^2\right)S\langle r\phi\rangle = 0, \tag{2.15}$$

$$R(-\Phi - \rho g R\sin\phi) + \left(R_\phi S\langle r\phi\rangle - RS\langle rr\rangle\right) + \sigma R\chi = 0, \tag{2.16}$$

where $R(\phi,t)$ satisfies the constant volume constraint (2.10). In section 4 we relate $\boldsymbol{S}$ to $\boldsymbol{V}$.

Our problem may also be formulated for flows coating the outside of the cylinder. In this case we merely change the sign of D in (2.10) and the sign of the first and last of the three terms on the left of (2.15).

It will simplify later calculations to note here that the stress in a Newtonian fluid is given by

$$\boldsymbol{S} = \mu \boldsymbol{A}, \tag{2.17}$$

where

$$\begin{aligned}
&A\langle rr\rangle = 2u_r = 2\left(\frac{1}{r}\psi_\phi\right)_r,\\
&A\langle r\phi\rangle = \frac{1}{r}u_\phi + r\left(\frac{v}{r}\right)_r = \frac{1}{r^2}\psi_{\phi\phi} - r\left(\frac{\psi_r}{r}\right)_r,\\
&A\langle\phi r\rangle = A\langle r\phi\rangle,\\
&A\langle\phi\phi\rangle = 2\left(\frac{1}{r}v_\phi + \frac{u}{r}\right) = 2\left(-\frac{1}{r}\psi_{\phi r} + \frac{\psi_\phi}{r^2}\right).
\end{aligned} \tag{2.18}$$

In the Newtonian case the following problem governs $\psi(r,\phi,t)$ and $\Phi(r,\phi,t)$:

$$\rho\left\{\operatorname{curl}\left[\left(\psi_t - \mu\nabla^2\psi\right)\boldsymbol{e}_z\right] + \tfrac{1}{2}\nabla(\nabla\psi)^2 - \begin{bmatrix}\psi_r\nabla^2\psi\\ \frac{1}{r}\psi_\phi\nabla^2\psi\end{bmatrix}\right\} = \nabla\Phi \quad \text{in } \mathcal{V}(t). \tag{2.19}$$

At the outer cylinder, (2.13) must be satisfied, and on the free surface $r = R(\phi,t)$, we have (2.14) and

$$4R^3R_\phi\left(\frac{1}{r}\psi_\phi\right)_r + \left(R^2 - R_\phi^2\right)\left[\psi_{\phi\phi} - r^3\left(\frac{\psi_r}{r}\right)_r\right] = 0 \tag{2.20}$$

and

$$\Phi + \rho g R\sin\phi + 2\mu\left(\frac{2R_\phi^2}{R^2 - R_\phi^2} + 1\right)\left(\frac{1}{r}\psi_\phi\right)_r - \sigma\chi = 0, \tag{2.21}$$

where $R(\phi,t)$ satisfies the constant volume constraint (2.10). The Newtonian

problem just listed was solved in the steady case using perturbations by Ruschak and Scriven [1] and numerically by Orr and Scriven [5].

3. The perturbation equations in the steady case

The location of the free surface $r = R(\phi)$ is an unknown of the problem. It is convenient to work in the fixed domain between two circles which the fluid would occupy with $\Omega \neq 0$ and $g = 0$,

$$\mathcal{V}_0 = \{r_0, \phi \mid R_0 - D \leqslant r_0 \leqslant R_0, 0 \leqslant \phi < 2\pi\}. \tag{3.1}$$

We map $\mathcal{V}(t)$ into $\mathcal{V}_0$ with a mapping function

$$r = \tilde{r}(r_0,\phi) = R_0 + \frac{(R_0 - r_0)}{D}\big[R(\phi) - R_0\big], \tag{3.2}$$

which maps boundary points into boundary points

$$\tilde{r}(R_0,\phi) = R_0, \quad \tilde{r}(R_0 - D,\phi) = R(\phi).$$

The same map works in the unsteady case with $R(\phi,t)$ instead of $R(\phi)$.

Suppose that the domain $\mathcal{V}(t,\epsilon)$ and $R(\phi,\epsilon)$ depend on a parameter ϵ, and $\mathcal{V}(t,0) = \mathcal{V}_0$ and $R(\phi,0) = R_0 - D$. This will be true for our problem with ϵ proportional to a Reynolds number times a Froude number (see section 5); that is, with $\epsilon \propto g$. We define two types of derivatives:

$$H^{[n]}(r_0,\phi) = \frac{\mathrm{d}^n}{\mathrm{d}\epsilon^n} H\big(\tilde{r}(r_0,\phi,\epsilon),\phi,\epsilon\big)\big|_{\epsilon=0, r=r_0}$$

holding r_0 fixed, and

$$H^{\langle n\rangle}(r_0,\phi) = \frac{\partial^n}{\partial\epsilon^n} H(r,\phi,\epsilon)\big|_{\epsilon=0, r=r_0}$$

holding r fixed. The two derivatives are related by the chain rule, e.g. $R^{[n]} \equiv R^{\langle n\rangle}$, $H^{[0]} \equiv H^{\langle 0\rangle}$

$$H^{[1]} = H^{\langle 1\rangle} + R^{[1]} H_r^{\langle 0\rangle},$$

$$H^{[2]} = H^{\langle 2\rangle} + 2R^{[1]} H_r^{\langle 1\rangle} + R^{2[1]} H_{rr}^{\langle 0\rangle} + R^{[2]} H_r^{\langle 0\rangle}.$$

The eqns. (2.11)–(2.12) are identities in r and they hold when differentiated partially holding r fixed, but total derivatives $(\cdot)^{[n]}$ are required for equations (2.14)–(2.16) at the free boundary.

We find the functions

$$\psi^{\langle n\rangle}(r_0,\phi), \quad V^{\langle n\rangle}(r_0,\phi), \quad \Phi^{\langle n\rangle}(r_0,\phi), \quad S^{\langle n\rangle}(r_0,\phi), \quad R^{[n]}(\phi)$$

by solving perturbation problems in $\mathcal{V}_0$. Then the solution is constructed as a

Taylor series

$$\psi(r,\phi,\epsilon)=\sum_{n=0}^{\infty}\psi^{[n]}(r_0(r,\phi),\phi)\frac{\epsilon^n}{n!}=\sum_{n=0}^{\infty}\psi^{\langle n\rangle}(r,\phi)\frac{\epsilon^n}{n!},$$

$$R(\phi,\epsilon)=\sum_{n=0}^{\infty}R^{[n]}\frac{\epsilon^n}{n!} \tag{3.3}$$

etc.,
with r in $\mathcal{V}(t,\epsilon)$, $R(\phi,\epsilon)\leqslant r\leqslant R_0$ (see [7]). When $\epsilon=0$ ($g=0$) the fluid coating the inside of the cylinder moves as a rigid body and the stress is zero;

$$V^{\langle 0\rangle}(r_0,\phi)=\Omega r_0 e_\phi,$$

$$\psi^{\langle 0\rangle}(r_0,\phi)=\frac{\Omega}{2}\left(R_0^2-r_0^2\right),$$

$$\Phi^{\langle 0\rangle}(r_0,\phi)=-p^{\langle 0\rangle}(r_0,\phi)+p_a,$$

$$p^{\langle 0\rangle}(r_0,\phi)=\frac{\rho\Omega^2}{2}\left[r_0^2-(R_0-D)^2\right]-\frac{\sigma}{R_0-D},$$

$$R^{[0]}(\phi)=R_0-D. \tag{3.4}$$

When the fluid coats the outside of the cylinder we change the sign of σ and D. For future use, we note that on rigid motions $F_t^{\langle 0\rangle}(\tau)$ is independent of r_0 and ϕ, so

$$F_t^{\langle 0\rangle}(\tau)=Q(\tau) \tag{3.5}$$

is orthogonal and $\chi^{\langle 0\rangle}(x,\tau)=Q(\tau)x$.

Now we write the perturbation at first and second order, where for convenience in computation $\epsilon=g$. At first order

$$-\rho\Omega\left\{\operatorname{grad}\left(r_0\psi_r^{\langle 1\rangle}\right)-\begin{bmatrix} r_0\nabla^2\psi^{\langle 1\rangle}+2\psi_r^{\langle 1\rangle} \\ \dfrac{2}{r_0}\psi_\phi^{\langle 1\rangle}\end{bmatrix}\right\}$$

$$=\nabla\Phi^{\langle 1\rangle}+\operatorname{div}S^{\langle 1\rangle}\qquad\text{in }\mathcal{V}_0, \tag{3.6}$$

$$\psi^{\langle 1\rangle}(R_0,\phi)=\psi_r^{\langle 1\rangle}(R_0,\phi)=0. \tag{3.7}$$

The free surface equations at first order

$$\psi_\phi^{\langle 1\rangle}-\Omega r_0 R_\phi^{[1]}=0,$$

$$S^{\langle 1\rangle}\langle r\phi\rangle=0,$$

$$-\Phi^{\langle 1\rangle}+\rho\Omega^2 r_0 R^{[1]}-S^{\langle 1\rangle}\langle rr\rangle+\sigma\chi^{[1]}=\rho r_0\sin\phi \tag{3.8}$$

are evaluated at $r_0 = R_0 - D$. The constant volume condition (2.10) requires that

$$\int_0^{2\pi} R^{[1]}(\phi)\,\mathrm{d}\phi = 0. \tag{3.9}$$

At second order,

$$\rho\left\{\operatorname{grad}\left[-\Omega r_0 \psi_r^{\langle 2\rangle} + \left(\nabla\psi^{\langle 1\rangle}\right)^2\right] + \begin{bmatrix} \Omega r_0 \nabla^2\psi^{\langle 2\rangle} + 2\Omega\psi_r^{\langle 2\rangle} - 2\psi_r^{\langle 1\rangle}\nabla^2\psi^{\langle 1\rangle} \\ \Omega\dfrac{2}{r_0}\psi_\phi^{\langle 2\rangle} - \dfrac{2}{r_0}\psi_\phi^{\langle 1\rangle}\nabla^2\psi^{\langle 1\rangle} \end{bmatrix}\right\}$$

$$= \nabla\Phi^{\langle 2\rangle} + \operatorname{div} \boldsymbol{S}^{\langle 2\rangle} \qquad \text{in } \mathcal{V}_0, \tag{3.10}$$

$$\psi^{\langle 2\rangle}(R_0,\phi) = \psi_r^{\langle 2\rangle}(R_0,\phi) = 0. \tag{3.11}$$

The free surface equations at second order

$$\psi_\phi^{\langle 2\rangle} - \Omega r_0 R_\phi^{[2]} + 2R^{[1]}\psi_{r\phi}^{\langle 1\rangle} + 2R_\phi^{[1]}\psi_r^{\langle 1\rangle} - 2r_0 R^{[1]}R_\phi^{[1]} = 0,$$

$$2r_0 R_\phi^{[1]}\left(S^{\langle 1\rangle}\langle rr\rangle - S^{\langle 1\rangle}\langle\phi\phi\rangle\right) + 2r_0^2 S_r^{\langle 1\rangle}\langle r\phi\rangle + r_0^2 S^{\langle 2\rangle}\langle r\phi\rangle = 0,$$

$$-\Phi^{\langle 2\rangle} - 2R^{[1]}\Phi_r^{\langle 1\rangle} + \rho\Omega^2\left(R^{[2]}R_0 + R^{[1]^2}\right) + \frac{2}{R_0}R_\phi^{[1]}S^{\langle 1\rangle}\langle r\phi\rangle$$

$$-S^{\langle 2\rangle}\langle rr\rangle - 2S_r^{\langle 1\rangle}\langle rr\rangle R^{[1]} + \sigma\chi^{[2]} = 2\rho R^{[1]}\sin\phi \tag{3.12}$$

are evaluated at $r_0 = R_0 - D$. The constant volume condition (2.10) at second order requires that

$$\int_0^{2\pi}\left[R^{[1]^2}(\phi) + R^{[0]}R^{[2]}(\phi)\right]\mathrm{d}\phi = 0. \tag{3.13}$$

We shall not study the second-order problem here. All the normal stress effects arise at second order.

4. Functional expression of the stress

When the motion is steady and rigid, $\boldsymbol{F}_t^{-1} = \boldsymbol{F}_t^{\mathrm{T}} = \boldsymbol{Q}(\tau)$ is an orthogonal tensor, $\boldsymbol{C}_t(\tau) = \boldsymbol{Q}(\tau)\boldsymbol{Q}^{\mathrm{T}}(\tau) = \boldsymbol{1}$ and $\boldsymbol{G}(s) = 0$. We simplify the problem of choosing a constitutive equation for the fluid by restricting our considerations to possibly unsteady motions in which $\boldsymbol{G}(s)$ is small. Then we represent the stress

$$\boldsymbol{S} = \mathop{\mathcal{F}}_{s=0}^{\infty}\left[\boldsymbol{G}(s)\right]$$

in a Taylor series of functional derivatives which we assume can be repre-

sented by integrals

$$\boldsymbol{S} = \boldsymbol{S}_{(0)} + \boldsymbol{S}_{(1)} + \boldsymbol{S}_{(2)} + \dots,$$

$$\boldsymbol{S}_{(0)} = \mathfrak{F}_{(0)}[0] = 0,$$

$$\boldsymbol{S}_{(1)} = \mathfrak{F}_{(1)}[0|\boldsymbol{G}(s)] = \int_0^\infty \dot{\boldsymbol{G}}(s)\boldsymbol{G}(s)\,\mathrm{d}s = -\int_0^\infty \boldsymbol{G}(s)\dot{\boldsymbol{G}}(s)\,\mathrm{d}s,$$

$$\boldsymbol{S}_{(2)} = \mathfrak{F}_{(2)}[0|\boldsymbol{G}(s)|\boldsymbol{G}(s)] = \int_0^\infty \int_0^\infty \gamma(s_1,s_2)\dot{\boldsymbol{G}}(s_1)\dot{\boldsymbol{G}}(s_2)\,\mathrm{d}s_1\,\mathrm{d}s_2. \tag{4.1}$$

We note that $\dot{\boldsymbol{G}}(s)$ in (4.1) may be written as $\dot{\boldsymbol{G}}(s,\epsilon)$ where $\epsilon = g$ is a perturbation of data $g = 0$ giving rise to steady rigid rotation $\boldsymbol{G}(s,0) = \boldsymbol{G}^{\langle 0\rangle}(s) = 0$. Then the expansion

$$\dot{\boldsymbol{G}}(s,\epsilon) = \epsilon\dot{\boldsymbol{G}}^{\langle 1\rangle}(s) + \tfrac{1}{2}\epsilon^2\dot{\boldsymbol{G}}^{\langle 2\rangle}(s) + \mathrm{O}(\epsilon^3)$$

gives rise to an expansion of the extra stress

$$\boldsymbol{S}(\epsilon) = \epsilon\boldsymbol{S}^{\langle 1\rangle} + \tfrac{1}{2}\epsilon^2\boldsymbol{S}^{\langle 2\rangle} + \mathrm{O}(\epsilon^3),$$

where

$$\boldsymbol{S}^{\langle 1\rangle} = -\int_0^\infty \boldsymbol{G}(s)\dot{\boldsymbol{G}}^{\langle 1\rangle}(s)\,\mathrm{d}s, \tag{4.2}$$

and

$$\boldsymbol{S}^{\langle 2\rangle} = -\int_0^\infty \boldsymbol{G}(s)\dot{\boldsymbol{G}}^{\langle 2\rangle}(s)\,\mathrm{d}s + 2\int_0^\infty \int_0^\infty \gamma(s_1,s_2)\dot{\boldsymbol{G}}^{\langle 1\rangle}(s_1)\dot{\boldsymbol{G}}^{\langle 1\rangle}(s_2)\,\mathrm{d}s_1\,\mathrm{d}s_2. \tag{4.3}$$

The computation of the tensors $\dot{\boldsymbol{G}}^{\langle n\rangle}(s)$ is complicated (see [3]) and will not be repeated here. The resulting equations have a simple form when expressed in cylindrical coordinates. Relative to cylindrical bases $\boldsymbol{e}_r(\phi)$, $\boldsymbol{e}_\phi(\phi)$ at time t,

$$\left[-\boldsymbol{G}^{\langle 1\rangle}(s)\right] = \begin{bmatrix} \hat{A}^{\langle 1\rangle}\langle rr\rangle & \hat{A}^{\langle 1\rangle}\langle r\phi\rangle \\ \hat{A}^{\langle 1\rangle}\langle \phi r\rangle & \hat{A}^{\langle 1\rangle}\langle \phi\phi\rangle \end{bmatrix}(s), \tag{4.4}$$

where the components are defined by (2.18) with $(\hat{u}^{\langle 1\rangle},\hat{v}^{\langle 1\rangle},\hat{\psi}^{\langle 1\rangle})$ replacing (u,v,ψ). The caret overbar has the following meaning: for any function $f(r,\phi,t)$ we define

$$\hat{f}(s) \equiv f(r,\phi-\Omega s,t-s). \tag{4.5}$$

In a similar way

$$\left[-\boldsymbol{G}^{\langle 2\rangle}(s)\right] = \begin{bmatrix} \hat{A}^{\langle 2\rangle}\langle rr\rangle & \hat{A}^{\langle 2\rangle}\langle r\phi\rangle \\ \hat{A}^{\langle 2\rangle}\langle \phi r\rangle & \hat{A}^{\langle 2\rangle}\langle \phi\phi\rangle \end{bmatrix}(s) + \begin{bmatrix} B\langle rr\rangle & B\langle r\phi\rangle \\ B\langle \phi r\rangle & B\langle \phi\phi\rangle \end{bmatrix}(s), \tag{4.6}$$

where the components of $\boldsymbol{B}$ are determined by $\hat{\psi}^{\langle 1\rangle}$ and are homogeneous of degree two in $\psi^{\langle 1\rangle}(r,\phi-\Omega s,t-s)$. Explicit forms for the components of $\boldsymbol{B}$ were given by Joseph [3] but they are not needed here.

Finally we note that for steady flow

$$\hat{f}(s)=f(r,\rho-\Omega s)$$

does not depend explicitly on time $t-s$.

5. Solution of the first order problem

To complete the specification of the first-order problem we need to specify the components of div $\boldsymbol{S}^{\langle 1\rangle}$ in (3.6), and $S^{\langle 1\rangle}\langle r\phi\rangle$, $S^{\langle 1\rangle}\langle rr\rangle$ and $\chi^{[1]}$ in (3.8):

$$\begin{aligned}\boldsymbol{e}_r\cdot\operatorname{div}\boldsymbol{S}^{\langle 1\rangle}&=\int_0^\infty G(s)\left[\left(\nabla^2-\frac{1}{r_0^2}\right)u^{\langle 1\rangle}(r_0,\phi-\Omega s)+\frac{2}{r_0^2}\frac{\partial v^{\langle 1\rangle}(r_0,\phi-\Omega s)}{\partial\phi}\right]\mathrm{d}s\\&=\left[\left(\nabla^2-\frac{1}{r_0^2}\right)\left(\frac{1}{r_0}\frac{\partial}{\partial\phi}\right)-\frac{2}{r_0^2}\frac{\partial}{\partial r_0}\frac{\partial}{\partial\phi}\right]\int_0^\infty G(s)\psi^{\langle 1\rangle}(r_0,\phi-\Omega s)\,\mathrm{d}s,\end{aligned}\tag{5.1}$$

$$\begin{aligned}\boldsymbol{e}_\phi\cdot\operatorname{div}\boldsymbol{S}^{\langle 1\rangle}&=\int_0^\infty G(s)\left[\frac{2}{r_0^2}\frac{\partial u^{\langle 1\rangle}(r_0,\phi-\Omega s)}{\partial\phi}+\left(\nabla^2-\frac{1}{r_0^2}\right)v^{\langle 1\rangle}(r_0,\phi-\Omega s)\right]\mathrm{d}s\\&=\left[\frac{2}{r_0^2}\frac{\partial^2}{\partial\phi^2}-\left(\nabla^2-\frac{1}{r_0^2}\right)\frac{\partial}{\partial r_0}\right]\int_0^\infty G(s)\psi^{\langle 1\rangle}(r_0,\phi-\Omega s)\,\mathrm{d}s,\end{aligned}\tag{5.2}$$

$$S^{\langle 1\rangle}\langle r\phi\rangle=\left(\frac{1}{r_0^2}\frac{\partial^2}{\partial\phi^2}-\frac{\partial^2}{\partial r_0^2}+\frac{1}{r_0}\frac{\partial}{\partial r_0}\right)\int_0^\infty G(s)\psi^{\langle 1\rangle}(r_0,\phi-\Omega s)\,\mathrm{d}s,\tag{5.3}$$

$$S^{\langle 1\rangle}\langle rr\rangle=2\left(\frac{1}{r_0}\frac{\partial^2}{\partial r_0\partial\phi}-\frac{1}{r_0^2}\frac{\partial}{\partial\phi}\right)\int_0^\infty G(s)\psi^{\langle 1\rangle}(r_0,\phi-\Omega s)\,\mathrm{d}s,\tag{5.4}$$

where (5.3) and (5.4) are evaluated at $r_0=R_0-D$ and

$$\chi^{[1]}=-\frac{\left(R^{[1]}-R^{[1]}_{\phi\phi}\right)}{(R_0-D)^2}.\tag{5.5}$$

Suppose $G(s)=\mu\delta(s)$ where μ is the viscosity and $\delta(s)$ is Dirac's function. Then

$$\int_0^\infty G(s)\psi^{\langle 1\rangle}(r_0,\phi-\Omega s)\,\mathrm{d}s=\mu\psi^{\langle 1\rangle}(r_0,\phi).\tag{5.6}$$

In this case we obtain the perturbation equations for a Newtonian fluid studied by Ruschak and Scriven [1]. Without assuming (5.6) we shall obtain a complex system of equations, identical to the ones we would get in the Newtonian case but with μ replaced by the complex viscosity $\eta^*(\Omega)$,

$$\eta^*(\Omega) = \int_0^\infty G(s)\, e^{-i\Omega s}\, ds.$$

To show this, we note that the driving term on the right of (3.8) may be expressed in complex form as

$$\rho(R_0 - D)\frac{e^{i\phi} - e^{-i\phi}}{2i},$$

so that we may obtain solutions in the form

$$\begin{bmatrix} \psi^{\langle 1\rangle}(r_0,\phi) \\ \Phi^{\langle 1\rangle}(r_0,\phi) \\ R^{[1]}(\phi) \end{bmatrix} = \tfrac{1}{2}\begin{bmatrix} f(r_0) \\ h(r_0) \\ r \end{bmatrix} e^{i\phi} + \text{conjugate.} \tag{5.7}$$

It follows immediately that $\chi^{[1]} = 0$ and (3.9) holds identically. Moreover

$$\int_0^\infty G(s)\psi^{\langle 1\rangle}(r_0,\phi - \Omega s)\, ds = \tfrac{1}{2}\eta^*(\Omega) f(r_0)\, e^{i\phi} + \text{conjugate.}$$

The equations governing $f(r_0), h(r_0)$ and r are obtained from (3.6),

$$\rho\Omega\left(2f' - \frac{1}{r}f\right) = h' + i\eta^*(\Omega)\frac{1}{r_0}\mathcal{L}f, \tag{5.8}$$

$$i\rho\Omega\left(-f' + \frac{2}{r_0}f\right) = \frac{i}{r_0}h - \eta^*(\Omega)[\mathcal{L}f]'; \tag{5.9}$$

and from (3.7),

$$f(R_0) = f'(R_0) = 0; \tag{5.10}$$

and from (3.8),

$$f - \Omega(R_0 - D)r = 0,$$

$$\frac{f}{(R_0 - D)^2} + f'' - \frac{1}{(R_0 - D)}f' = 0,$$

$$-h + \rho\Omega^2(R_0 - D)r - \frac{2i\eta^*(\Omega)}{R_0 - D}\left(f' - \frac{f}{R_0 - D}\right) = \frac{\rho(R_0 - D)}{i}. \tag{5.11}$$

Equations (5.8)–(5.11) are the same as the ones which hold for Newtonian fluids with viscosity μ replacing $\eta^*(\Omega)$.

After eliminating h from (5.8), (5.9) and $(5.11)_3$, we find that $f(r_0)$ satisfies

$$\mathcal{L}^2 f - \mathrm{i}\frac{\rho\Omega}{\eta^*}\mathcal{L}f = 0 \qquad \text{in } \mathcal{V}_0,$$

$$f(R_0) = f'(R_0) = 0, \tag{5.12}$$

where

$$\mathcal{L} = \frac{\mathrm{d}^2}{\mathrm{d}r_0^2} + \frac{1}{r_0}\frac{\mathrm{d}}{\mathrm{d}r_0} - \frac{1}{r_0^2}.$$

At $f_0 = R_0 - D$ we must satisfy $(5.11)_2$ and

$$\left(\frac{3}{r_0^2} + \frac{\mathrm{i}\rho\Omega}{\eta^*(\Omega)}\right) r_0 f'' - f''' = \frac{\rho}{\eta^*(\Omega)}. \tag{5.13}$$

Equations $(5.11)_2$ and (5.13) determine $f(r_0)$ uniquely. With $f(r_0)$ so determined, we may compute h from (5.9) and r from $(5.11)_1$.

It is instructive to write (5.12) and (5.13) in dimensionless form. We define

$$x = \frac{r_0}{R_0}, \qquad x_0 = \frac{R_0 - D}{R_0} \leqslant x \leqslant 1,$$

$$f(r_0) = \frac{R}{\Omega}\mathcal{F}(x),$$

$$\mathcal{R}(\Omega) = \frac{\rho\Omega R_0^2}{\eta^*(\Omega)}. \tag{5.14}$$

Then

$$\mathcal{L}^2\mathcal{F} - \mathrm{i}\mathcal{R}(\Omega)\mathcal{L}\mathcal{F} = 0,$$

$$\mathcal{F}(1) = \mathcal{F}'(1) = 0, \tag{5.15}$$

where

$$\mathcal{L} = \frac{\mathrm{d}^2}{\mathrm{d}x^2} + \frac{1}{x}\frac{\mathrm{d}}{\mathrm{d}x} - \frac{1}{x^2}.$$

At $x_0 = (R_0 - D)/R_0$, we must satisfy

$$\mathcal{F}'' - \frac{\mathcal{F}'}{x_0} + \frac{\mathcal{F}}{x_0^2} = 0 \tag{5.16}$$

and

$$\left(\frac{3}{x_0^2} + \mathrm{i}\mathcal{R}(\Omega)\right) x_0 \mathcal{F}'' - \mathcal{F}''' = \mathcal{R}(\Omega). \tag{5.17}$$

Equations (5.15)–(5.17) show that $\mathcal{F} = \mathcal{F}(x, \mathcal{R}(\Omega))$ depends on one complex

dimensionless parameter $\mathcal{R}(\Omega)$. For small $\mathcal{R}$, $\mathcal{F}(x,\mathcal{R})$ is a function of order $\mathcal{R}$.

The free surface equation $(5.11)_1$ may be made dimensionless with R_0

$$r=\frac{f}{\Omega(R_0-D)}=\frac{R_0}{\Omega^2(R_0-D)}\mathcal{F}(x_0), \tag{5.18}$$

and

$$R(\phi)=R_0-D+\tfrac{1}{2}(r\,e^{i\phi}+\bar{r}\,e^{-i\phi})g+O(g^2),$$

$$\frac{R(\phi)}{R_0-D}=1+Fr\{\mathcal{F}(x,\mathcal{R})\,e^{i\phi}+\bar{\mathcal{F}}(x,\mathcal{R})\,e^{-i\phi}\}+O(Fr^2),$$

where $Fr=gR_0/\Omega^2(R_0-D)^2$ is a Froude number. In section 7, we argue that the perturbation of the free surface is small when

$$Fr|\mathcal{R}(\Omega)|\frac{D^2}{R_0^2}\ll 1. \tag{5.19}$$

The solution of (5.15)–(5.17) is elementary. We write this solution, using $d=D/R_0$, as

$$\mathcal{F}(x)=k_1x+k_2\frac{1}{x}+k_3J_1(\alpha x)+k_4Y_1(\alpha x),$$

$$\alpha=(\tfrac{1}{2}\mathcal{R}(\Omega))^{1/2}(1-i), \tag{5.20}$$

where J_1 and Y_1 are two kinds of Bessel functions, and

$$k_1=-\frac{i}{2}(1-d)^2-k_3J_1(\alpha)-k_4Y_1(\alpha),$$

$$k_2=\frac{i}{2}(1-d)^2,$$

$$k_3=i(1-d)[a_2-(1-d)a_4]/[a_1a_4-a_2a_3],$$

$$k_4=i(1-d)[(1-d)a_3-a_1]/[a_1a_4-a_2a_3],$$

$$a_1=2J_1(\alpha)-\alpha J_0(\alpha),$$

$$a_2=2Y_1(\alpha)-\alpha Y_0(\alpha),$$

$$a_3=(2-\tfrac{1}{2}\alpha_1^2)J_1(\alpha_1)-\alpha_1J_0(\alpha_1),$$

$$a_4=(2-\tfrac{1}{2}\alpha_1^2)Y_1(\alpha_1)-\alpha_1Y_0(\alpha_1),$$

$$\alpha_1=\alpha(1-d).$$

Ruschak and Scriven [1] solved this problem for real values of $\mathcal{R}(\Omega)$. In the real case the solution can be simplified by using Kelvin or Thompson functions.

6. The complex viscosity

If the density is constant then the only "material parameter" on which our solution depends is $\eta^*(\Omega)$. In fact, one useful experimental test of our theory, assuming small $Fr|\mathcal{R}(\Omega)|$, is that for a certain fluid one and only one "smooth" complex function should be determined for different values of R_0, D and Ω. We have also showed that under these same conditions the internal motion is determined by Ω through $\mathcal{R}(\Omega)$ and is independent of Fr. Under the same conditions the free surface and the internal motion are independent of surface tension.

The complex viscosity is a complex function which is usually represented as

$$\eta^*(\Omega) \equiv \eta'(\Omega) - i\eta''(\Omega) \equiv \int_0^\infty G(s)\, e^{-i\Omega s}\, ds, \tag{6.1}$$

where $\eta'(\Omega)$ is the dynamic viscosity and $\eta''(\Omega)$ is the elastic storage modulus. $\eta^*(\Omega)$ is uniquely determined by the shear relaxation modulus $G(s)$. This modulus is a material parameter but $\eta^*(\Omega)$, which depends on *dynamics*, is not a material parameter. In a Newtonian fluid $\eta'(\Omega) = \mu$ (a constant) and $\eta''(\Omega) = 0$ for all Ω. For Newtonian fluids $\eta^*(\Omega) = \mu$ is a material parameter. We shall call $\eta'(0) = \mu$ the zero-frequency viscosity.

Rheologists like $\eta^*(\Omega)$ because there are good experimental methods which can be used to determine it. One popular method uses the theory of response of fluids to small-amplitude oscillations of parallel plates. Another popular method uses the orthogonal rheometer. The flow in this last instrument also falls in the frame of rotating simple fluids [3,8].

Our experiment is yet another method. It is worth noting that in the orthogonal rheometer and in our experiment we find a quantity which depends on dynamics ($\eta^*(\Omega)$) from a steady flow. $\eta^*(\Omega)$ has been measured for a number of polymer solutions (for example, some values are given in [9]).

The analytical form of $\eta^*(\Omega)$ is determined by $G(s)$, and $G(s)$ varies from fluid to fluid. It is not likely that there is a universal form for $G(s)$ applicable to all fluids. However, in some situations, some kind of approximation to observations of $\eta^*(\Omega)$ when Ω is not too large can be obtained from Maxwell models, the simplest of which is the spring and dashpot model shown in Fig. 2.

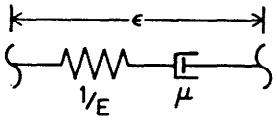

Fig. 2. Spring and dashpot Maxwell model. The spring constant is $1/E$ and the friction coefficient is μ.

The stress τ in the model of Fig. 2 is

$$\tau = \int_0^\infty \frac{1}{E} \dot{\epsilon}(t-s)\, e^{-1/\mu E}\, ds,$$

and

$$G(s) = \frac{1}{E}\, e^{-(1/E\mu)s},$$

$$\eta' = \frac{\mu}{1+\mu^2 E^2 \Omega^2},$$

$$\eta'' = \frac{E\Omega}{(1/\mu^2)+\Omega^2 E^2}. \tag{6.2}$$

It is sometimes useful to express E in terms of the Rivlin–Ericksen constant α_1 (α_1 is one of two constants describing fluids of second grade);

$$\alpha_1 = -\mu^2 E \leqslant 0, \qquad G(s) = -\frac{\mu^2}{\alpha_1}\, e^{\mu s/\alpha_1}.$$

In our experiments for example, we have a fluid with $\mu = 200$ poise and $\alpha_1 = -50\,\mathrm{g\,cm^{-1}}$. When Ω is small, the other parameters being fixed, we get

$$\eta' = \mu,$$

$$\eta'' = \mu^2 E\Omega = -\alpha_1 \Omega \qquad (\Omega \text{ small}). \tag{6.3}$$

On the other hand when $E\Omega$ or η is large,

$$\eta' = \frac{1}{\mu E \Omega^2} = -\frac{\mu}{\alpha_1 \Omega^2},$$

$$\eta'' = \frac{1}{\Omega E} \qquad (\text{Large } E\Omega \text{ or large } \mu). \tag{6.4}$$

So the two-element model predicts that the elastic response is equal to $1/E$ and that the viscous contribution decays to zero faster than the elastic one, whenever one of the two limits specified in (6.4) holds.

Returning now to the exact expression (6.1) for $\eta^*(\Omega)$, we record its polar form in the following notation

$$\eta^*(\Omega) = |\eta^*(\Omega)|\, e^{i \arg \eta^*(\Omega)},$$

$$\Theta = -\arg \eta^*(\Omega) = \arctan\left(\frac{\eta''(\Omega)}{\eta'(\Omega)}\right),$$

$$\frac{1}{\eta^*(\Omega)} = \frac{1}{|\eta^*(\Omega)|}\, e^{i\Theta}. \tag{6.5}$$

7. Asymptotic form of the solution for small $|\mathcal{R}|$

To allow a direct interpretation of our solution we shall also assume that the average film thickness $d << 1$. Then

$$\mathcal{F}(x) = d^3 \mathcal{R}(\Omega)\left(\frac{y^3}{6} - \frac{y^2}{2}\right), \tag{7.1}$$

where $y = (1-x)/d$. Using (7.1) we may form expressions for the velocity, pressure and free surface. Returning finally to the original dimensional variables, we find that

$$u = \frac{\rho g}{6r_0}\left[3D(R_0 - r_0)^2 - (R_0 - r_0)^3\right]\left(\frac{1}{|\eta^*(\Omega)|}\sin\left[\phi + \Theta(\Omega)\right]\right),$$

$$v = \Omega r_0 + \frac{\rho g}{2}\left[(R_0 - r_0)^2 - 2D(R_0 - r_0)\right]\left(\frac{1}{|\eta^*(\Omega)|}\cos\left[\phi + \Theta(\Omega)\right]\right),$$

$$p = \rho\Omega^2\left(r_0^2 - \left(R_0^2 - D^2\right) - \frac{\sigma}{R_0 - D}\right) + \rho g R_0 \Omega\left[D(R_0 - r_0) - \tfrac{1}{2}(R_0 - r_0)^2\right]$$

$$\times \quad \frac{1}{|\eta^*(\Omega)|}\cos\left[\phi + \Theta(\Omega)\right] + \frac{g}{\Omega^2 R_0^2}\left[D - (R_0 - r_0)\right]\sin\phi, \tag{7.2}$$

where $\Theta = \arctan[\eta''(\Omega)/\eta'(\Omega)]$. In (7.2), the velocity and the pressure are expressed in terms of the radius r_0, $R_0 - D \leq r_0 \leq R_0$, in the undeformed domain. They may be re-expressed in terms of the radius r of the deformed domain by the mapping function (3.1) and the expression

$$R_0 - R(\phi) = D + \frac{gD^3\rho}{3\Omega R_0 |\eta^*(\Omega)|}\cos\left[\phi + \Theta(\Omega)\right]. \tag{7.3}$$

Equation (7.3) shows that the perturbation of the free surface with $|\mathcal{R}(\Omega)|$ and D/R_0 small is small if

$$\frac{gD^2\rho}{3\Omega R_0 |\eta^*(\Omega)|} << 1. \tag{7.4}$$

Using a thin film lubrication approximation Moffatt [10] and Deiber and Cerro [6] found a similar solution for the Newtonian problem in which $\eta^*(\Omega)$ is constant and real. Their solution and ours are the same when $d^2 Fr \mathcal{R} << 1$.

8. Asymptotic form of the solution at large Ω

Using the large argument form for the Bessel functions in (5.20), we find

$$\mathcal{F}(x) = -\frac{\mathrm{i}}{2}(1-d)^2\left(x-\frac{1}{x}\right) + \frac{\mathrm{i}(1-d)^2}{\alpha\cos\alpha}\left[\sin\{\alpha[x-(1-d)]\} - x\sin(\alpha d)\right],$$

$$\alpha = \left(\frac{\mathcal{R}}{2}\right)^{1/2}(1-\mathrm{i}). \tag{8.1}$$

There is a *dramatic* difference between Newtonian and viscoelastic liquids for large Ω. This difference can be determined from the amplitude function $f'(x)$ of the azimuthal component of velocity

$$v^{(1)} = -f'(x)\,\frac{\mathrm{e}^{\mathrm{i}\phi}}{2} + \text{conjugate}.$$

In the Newtonian case $\mathcal{R} = R_0^2\Omega\rho/\eta$ is real and depends linearly on Ω and

$$\mathcal{F}' \sim -\frac{\mathrm{i}}{2}(1-d)^2\left(1+\frac{1}{x^2}\right) + \frac{(1-d)^2}{x^{1/2}}\left\{\exp\left[-(\mathcal{R}/2)^{1/2}(1-x)\right]\right.$$
$$\left.\times\left(\mathrm{i}\cos\left[(\mathcal{R}/2)^{1/2}(1-x)\right] - \sin\left[(\mathcal{R}/2)^{1/2}(1-x)\right]\right)\right\}. \tag{8.2}$$

The second term vanishes exponentially for large $\mathcal{R}$ except in a boundary layer near the cylinder wall at $x=1$. The flow is inviscid outside the boundary layer.

To determine the large Ω limit in the viscoelastic case we note that, after integrating (6.1) by parts, it is possible to show, without approximation, that

$$\eta^*(\Omega) = \frac{G(0)}{\mathrm{i}\Omega} - \frac{G'(0)}{\Omega^2} + O\left(\frac{1}{\Omega^3}\right). \tag{8.3}$$

For large Ω, we obtain

$$\alpha \sim \left(\frac{R_0^2\rho}{2G(0)}\right)^{1/2}\left(\Omega - \mathrm{i}\frac{G'(0)}{2G(0)}\right)$$

and

$$\mathcal{F}' = \frac{\mathrm{i}}{2}(1-d)^2\left(1+\frac{1}{x^2}\right) + \frac{\mathrm{i}(1-d)^2}{x^{1/2}\cos(\alpha d)}\cos\{\alpha[x-(1-d)]\}. \tag{8.4}$$

The viscoelastic contribution (the second term) does not vanish when $\Omega \to \infty$. The flow has *no* boundary layer. When expressed in terms of real dimension-

less variables, the azimuthal component of velocity is given by

$$v^{(1)} = -\frac{(1-d)^2}{2}\left(1+\frac{1}{r_0^2}\sin\phi\right)$$
$$+\frac{(1-d)^2}{\sqrt{r}}\left(\frac{\cos x\cosh y\cos x'\cosh y'+\sin x\sinh y\sin x'\sinh y'}{\cos^2 x+\sinh^2 y}\sin\phi\right.$$
$$\left.-\frac{\cos x\cosh y\sin x'\sinh y'-\sin x\sinh y\cos x'\cosh y'}{\cos^2 x+\sinh^2 y}\cos\phi\right) \quad (8.5)$$

(the velocity v is made dimensionless with $R_0(\Omega)$ and the free surface is given by

$$r^{[1]} = \left(\frac{d^2}{2}-d\right)\sin\phi-\frac{(1-d)^2 d}{\sqrt{1-d}}\left(\frac{x\sinh y\cosh y-y\sin x\cos x}{(x^2+y^2)(\cos^2 x+\sinh^2 y)}\cos\phi\right.$$
$$\left.+\frac{x\sin x\cos x+y\sinh y\cosh y}{(x^2+y^2)(\cos^2 x+\sinh^2 y)}\sin\phi\right), \quad (8.6)$$

where

$$x=\sqrt{\frac{R_0^2\rho}{G(0)}}\,\Omega d,$$
$$y=-\sqrt{\frac{R_0^2\rho}{G(0)}}\,d\frac{G'(0)}{2G(0)},$$
$$x'=\sqrt{\frac{R_0^2\rho}{G(0)}}\,\Omega[r_0-(1-d)],$$
$$y'=-\sqrt{\frac{R_0^2\rho}{G(0)}}\,\frac{G'(0)}{2G(0)}[r_0-(1-d)]. \quad (8.7)$$

Inspection of (8.6) and (8.7) shows that as $\Omega\to\infty$,

$$r^{[1]}=\left(\frac{d^2}{2}-d\right)\sin\phi,$$

so that the maximum film thickness is at $\Theta=90°$. The effect of increasing Ω is to move the maximum up towards the top of the cylinder.

The azimuthal component of the perturbation velocity vanishes as $\Omega\to\infty$, which can be seen after writing (8.5) in dimensions (multiply by $\epsilon\cdot R_0\Omega = g/\Omega$). Both the inviscid and the viscoelastic parts are of the same order and vanish like $1/\Omega$, but the viscoelastic part of the shear strain, $(\partial/\partial r)V^{(1)}$, does not vanish with increasing Ω.

9. Physical interpretation of the effects of fluid memory

The effects of the fluid memory are most easily described when $|\mathcal{R}(\Omega)|$ is small. A purely Newtonian liquid will be slowed down by gravity on the rising side of the cylinder, resulting in an increased thickness on that side. Acceleration on the falling side has the opposite effect. The flow is balanced by viscous forces which act against the acceleration due to gravity (Fig. 3). The viscoelastic liquid has a memory for viscous forces, but the forces due to gravity are not changed by the fluid memory. The effect of the fluid memory is to let the viscous forces act longer, which means roughly that the whole pattern of viscous forces rotates in the direction of rotation (Fig. 3). This rotation produces a faster flow and a smaller film thickness in the first quadrant. We can see what happens by inspecting $(7.2)_2$ and (7.3). In the viscoelastic case, $\Theta(\Omega)$ is positive and $0 \leqslant \Theta \leqslant \pi/2$, so positions ϕ of constant phase ($\phi + \Theta(\Omega) = \text{constant}$) are all rotated through $-\Theta(\Omega)$. In the Newtonian case $\Theta = 0$ for all Ω.

The same effect can be explained in terms of an elastically dominated response in which $\eta'(\Omega)/\eta''(\Omega) \to 0$ (large Ω, small $\mathcal{R}(\Omega)$ for example). In this case, viscous forces are small relative to elastic ones and gravity causes the fluid to sag at the bottom,

$$\Theta(\Omega) = \pi/2, \qquad \cos(\phi + \pi/2) = 1 \qquad \text{at } \phi = -\pi/2.$$

So, in the general case we have something between the purely viscous case with maximum thickness at $\phi = 0$ and the elastic case with maximum thickness at $\phi = -\pi/2$.

10. Limits of validity of the perturbation solution

Our formal analysis does not allow us to establish the limits of validity of the perturbation theory. The analysis of section 7 suggests that the perturba-

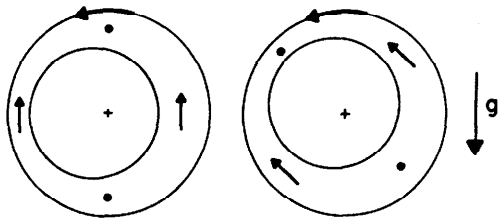

Fig. 3. Viscous forces: (left) Newtonian liquid, (right) viscoelastic liquid. The angle of maximum thickness moves to the fourth quadrant for a viscoelastic liquid.

tion solution should be an approximation to the true solution when

$$\frac{gD^2\rho}{3\Omega R_0|\eta^*|} << 1.$$

In the Newtonian case it is possible to compare the perturbation solution [1] with an exact numerical solution of Orr and Scriven [5]. These authors find [5, p. 158]:"What is remarkable is the agreement between the numerical and asymptotic solutions when the gravity parameter is not small. Even for $g/\Omega^2 R_0 = 2.0$ the free-surface locations differ only in the third decimal. Ruschak's solutions at first order in gravity are quite accurate for the parameter set shown in figure 2 [of [5]] (i.e. $\mathcal{R} = R_0^2\Omega\rho/\eta = 1$, $S = \sigma/\rho\Omega^2 R_0^3 = 1$, $d = 0.5$). At higher Reynolds number, however, the agreement deteriorates more rapidly with increasing gravity." They also find that the solutions differ qualitatively for large $\mathcal{R}$, when the surface tension parameter $S = \sigma/\rho\Omega^2 R_0^3$ is not small. In that case, the numerical solution shows that the angle between the maximum and minimum film thicknesses is no longer 180°.

11. Experimental equipment and procedures

The experimental apparatus was designed to provide a continuous record of the thickness of a film of liquid coating the inside of a horizontal rotating cylinder as a function of the circumferential position. The real and imaginary parts of the complex viscosity $\eta^*(\Omega)$ are then determined as functions of the angular speed Ω from the measured circumferential variation of film thickness. The results are tested by comparing the values obtained for $\eta^*(\Omega)$ at several different average film thickness levels d, and we say that the linear theory governs the experiment when the data determine a unique $\eta^*(\Omega)$, independent of d.

We also compare the values of $\eta^*(\Omega)$ with the corresponding values obtained from independent experiments performed on a Rheometrics Dynamic Spectrometer, using the oscillating cone- and- plate configuration.

11.1 The experimental equipment

The principal features of the equipment are shown schematically in Fig. 4. The central component is a Plexiglas cylinder which rotates about its horizontal axis. The cylinder contains a predetermined volume of the test liquid, which coats the inside wall of the cylinder as it rotates. A light absorption technique is used to measure the thickness of the liquid film. A narrow beam of light from a laser is passed through the liquid film and impinges on a photodiode fastened to the outside of the cylinder. The

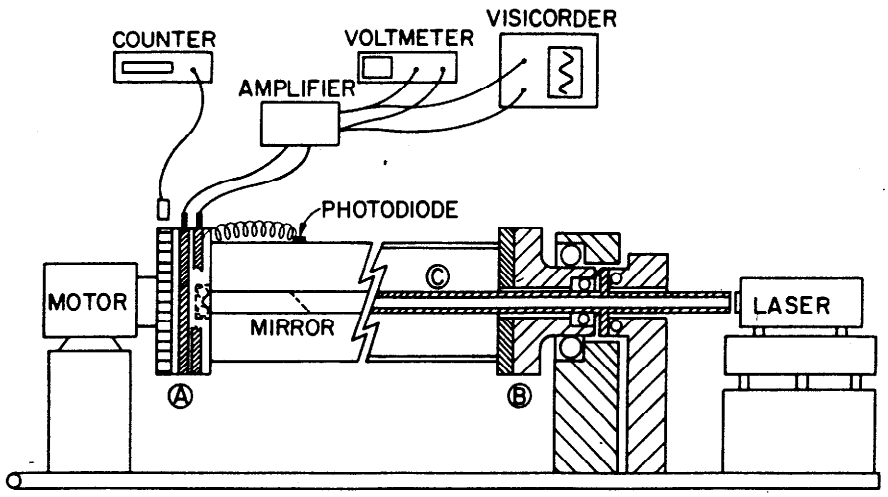

Fig. 4. Schematic view of the experimental apparatus.

electrical signal from the photodiode is amplified in a differential amplifier to increase measurement sensitivity, after which it is displayed on an oscilloscope and/or on a visicorder, thus producing a continuous record of film thickness as a function of angular position.

The Plexiglas cylinder has an inner diameter of 6.45 cm and an outer diameter of 7.58 cm. It is 60.5 cm long, with a Plexiglas flange at each end. The ends of the cylinder are sealed by means of aluminum end-plates (indicated by A and B in Fig. 4) which bolt onto the flanges. The outer face of one end-plate (A) is fastened directly to the drive-shaft of the driving motor. This end-plate has 100 equally spaced slots machined into the outer edge, and is used in conjunction with a Kaman proximity gauge to measure the rotational speed.

A thrust bearing is countersunk into the inside face of end-plate A, and is accurately aligned with the axis of the cylinder. This bearing supports one end of a hollow brass tube C which is concentric with the cylinder. Two brass slip-rings are inlaid in the outer edge of the flange A. Carbon brushes are used with the slip-rings to transmit the electrical signal from the rotating photodiode to the stationary measuring system.

The outer aluminum end-plate (B) has a short hollow shaft on its external face. This shaft rides in a bearing located in a vertical support stand which forms part of the main frame of the apparatus. A second bearing is fixed inside the shaft, and is used to support the tube C which passes through this bearing. The tube is locked into place relative to the cylinder by means of a locating pin which is attached to a collar on the tube and which fits into a

hole in the shaft of the end-plate B. Thus the tube C and the cylinder rotate together. The tube is restrained from movement in the axial direction by means of a second support stand which bears upon a thrust bearing attached to the collar.

The purpose of the hollow tube C is to direct a radial beam of light from the inside of the cylinder onto the photodiode attached to the outside of the cylinder. This is accomplished by means of a small front-surfaced mirror which is mounted in the tube at 45° to the axis. A laser beam is directed along the tube and is reflected in a radial direction by the mirror. A small hole in the tube, approximately 6 mm in diameter and 28 cm from the closed end, allows the light to pass in the radial direction. The outer diameter of the tube is 11.3 mm, and the tube projects about 25 cm outside the end-plate B.

The driving motor is an Electrocraft Motomatic Type 650 d.c. servo-motor with a feedback control system. The mechanical parts of the equipment, including the laser and the driving motor, are mounted on a rigid aluminum frame. The frame is hinged at one end so that the entire system can be turned through 90° in a vertical plane. This allows the cylinder to be positioned vertically during the filling and emptying operations. The photographs of Fig. 5 show the equipment in the horizontal operating position and in the vertical filling position.

11.2 The electro-optical measurement system

The radial laser beam emerging from the hole in the brass tube (Fig. 4) passes through the liquid film where some absorption of the light takes place, and then impinges upon the photodiode attached to the outer wall of the cylinder. The photodiode emits a voltage which depends upon the intensity of the light impinging upon it.

Light absorption is governed by the Beer–Lambert law

$$I = I_0 \, e^{-kD},$$

where I is the intensity of the penetrating light, I_0 is the intensity of the incident light and D is the thickness of the absorbing film. To obtain a voltage output which varies linearly with the film thickness D, the photodiode is used in the photovoltaic mode with a high load resistance ($10^{12}\,\Omega$). This produces an output voltage which varies logarithmically with the intensity of the light impinging upon the photodiode.

The circumferential variations in the thickness of the liquid film are small, resulting in correspondingly small variations in signal voltage from the photodiode. In order to increase the sensitivity of the measuring technique, a differential amplifier circuit is used to subtract the voltage corresponding to the average film thickness from the signal voltage. The output voltage from

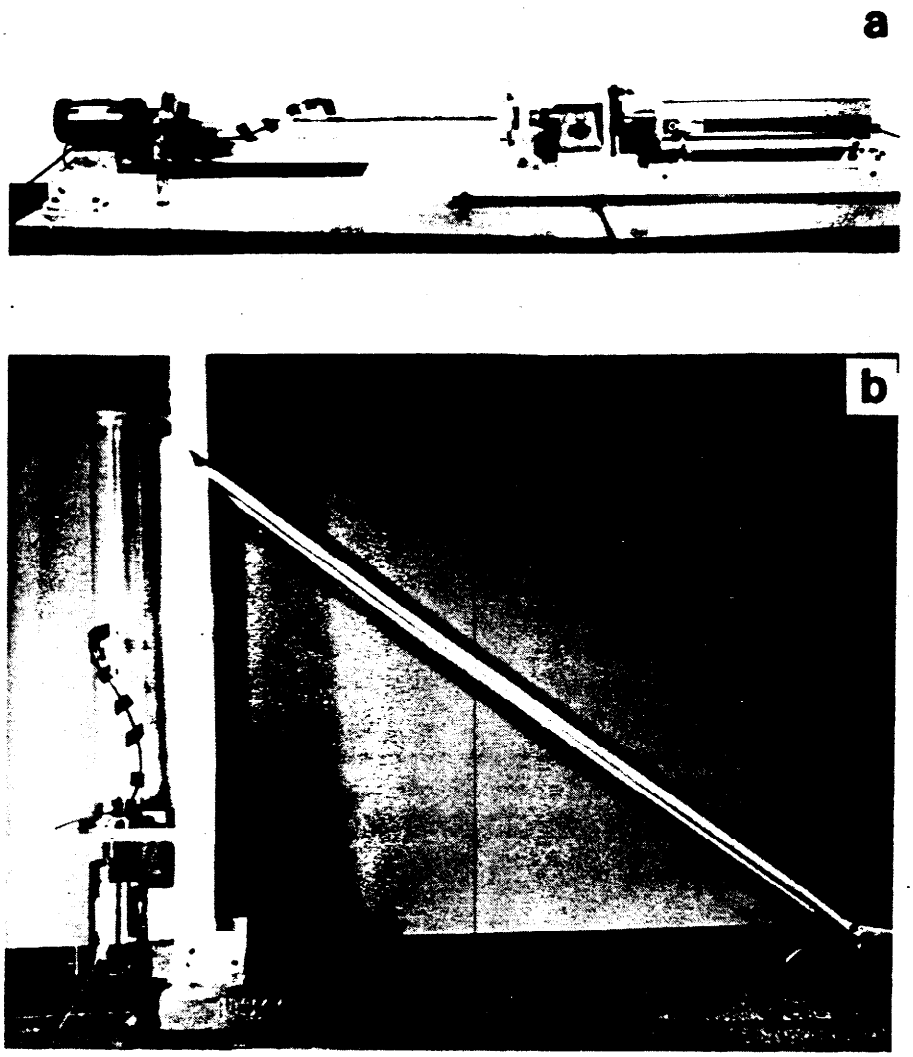

Fig. 5. The experimental apparatus: (a) horizontal operating position, (b) vertical filling position.

the differential amplifier thus gives a measure of the variation in film thickness relative to the average film thickness. Details concerning the electric circuitry may be found elsewhere [11].

In order to interpret the record of the output voltage in terms of the variation in film thickness, it is necessary to identify a point on the output data which corresponds to a known angular orientation of some point on the cylinder wall. This is accomplished by means of a microswitch located at a

fixed position on the main frame and a trigger fastened to the motor end-plate (A). The microswitch generates a single pulse which is recorded on the output trace.

The technique used in this experiment for measuring the angular variation of the film thickness has several advantages over a system in which the photodiode is located at a fixed position in space. Because the photodiode is fixed at the same position on the cylinder and rotates with the cylinder, a complete record of the angular variation of film thickness is generated during a single revolution of the cylinder. Thus the measurement can be made in a very short time interval and is not likely to be affected by any small changes in operating conditions. This technique also eliminates potential variations in light absorption caused by non-uniformities in the wall thickness of the cylinder.

Two small difficulties were encountered during the course of the experimental program. It was found that after some time in operation the Plexiglas cylinder began to exhibit a slight warping, so that a small eccentricity could be detected in the rotation of the cylinder about its axis. In the vicinity of the photodiode, the measured variation in the radius was $\pm 1.0\%$ of the mean inner radius of the cylinder.

It was also observed that the laser light exhibited small, slowly varying changes in intensity during operation. This had no effect during the short time in which film thickness measurements were being made, but could cause some fluctuations in the data during the calibration process which requires a longer time.

11.3 The liquids

Two different liquids were used for these experiments, namely STP, which is a solution of polyisobutylene in petroleum oil, and TLA 227, which is a solution of a methacrylate copolymer in oil. Both STP and TLA 227 have been used extensively for free surface experiments by Joseph, Beavers and co-workers in the past few years. The characteristics of these liquids have been well documented (e.g. [12–15]), and it is known that there is some batch-to-batch variations in density and climbing constant, particularly for STP. The fluid characteristics of the two samples used for the present experiments are given in Table 1. It should be noted that only the density values are required in the computations of η' and η''.

Both TLA 227 and STP are essentially transparent in thin films, so that it is necessary to add a small quantity of white paint pigment (titanium dioxide) to increase the opaqueness of each. The paint pigment is added in small increments to the main body of the test liquid (about 2 l). At each step the opaqueness of the liquid is tested using the system shown in Fig. 6. The

TABLE 1
Sample characteristics

	TLA 227	STP
Density (g cm^{-3})	0.896	0.890
Surface tension (dyn cm^{-1})	30.5	30.9
Shear viscosity (poise)	200	120

opaqueness of the liquid is increased until the maximum voltage change is registered for a fixed change in film thickness Δh. This is of the order of 0.2 to 0.3 V mm^{-1} for the liquids used in these experiments.

11.4 Calibration and measurements

The calibration of the output signal as a function of film thickness is performed during the course of a series of experimental runs at different average film thicknesses.

The experiment begins with the empty cylinder rotating at a high rotational speed (approximately $\Omega = 20$ rev s^{-1}), and the off-set voltage is adjusted to produce zero output voltage. A known small volume of liquid is added to the cylinder and it is again rotated at high speed. The average output voltage is recorded, and then the off-set voltage is immediately adjusted to bring the average output voltage back to zero. The rotational speed is then reduced to a much lower value and the angular variation of film thickness is recorded at several different low rotation speeds. After this, a further known volume of liquid is added to that already in the cylinder and the series of measurements is repeated. The whole cycle of operations is

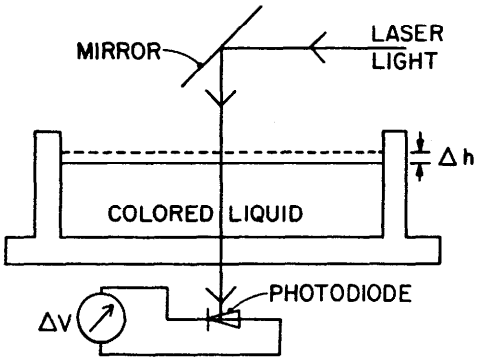

Fig. 6. Test system designed to optimize the amount of dye added to the liquid. Raising the liquid level by Δh results in a voltage output change.

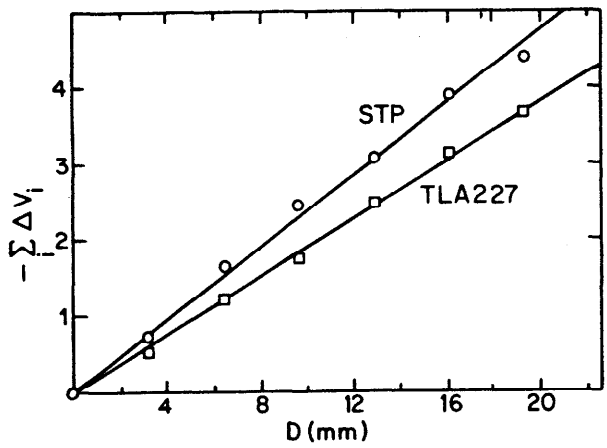

Fig. 7. Calibration data for STP and TLA 227. The output voltage varies linearly with the liquid thickness in the fast rotating cylinder.

repeated for several additional increments in the volume of liquid in the cylinder.

At the end of the experiment, a calibration graph is constructed from the high-rotation-rate data showing the output voltage increase as a function of increase in average film thickness. The calibration data for the samples of STP and TLA 227 used in this work are presented in Fig. 7. The output voltage varies linearly with film thickness over the ranges used in these experiments, and the calibration constants are $-0.24\,\mathrm{V\ mm^{-1}}$ for STP and $-0.189\,\mathrm{V\ mm^{-1}}$ for TLA 227.

12. Experimental results

12.1 Steady flow results

The values of $\eta'(\Omega)$ and $\eta''(\Omega)$ were computed using measurements taken from the output of the visicorder.

During the recording of the angular variations in film thickness, the gain of the visicorder was set as high as possible, and traces were recorded for several revolutions at each rotational speed in order to confirm the repeatability of the data. A typical visicorder output for TLA 227 is given in Fig. 8, which shows very clearly the sinusoidal-like variation of film thickness predicted by the theory. There is a small-amplitude, high-frequency noise superimposed on the main output signal. For most film thickness measurements, this noise presented no problems in the identification of the main signal trace and in measuring the appropriate amplitudes and phase angles.

Fig. 8. Typical visicorder output for TLA 227, showing the variation of liquid film thickness during one rotation.

The noise was most significant at high rotational speeds, when the variation in film thickness was very small.

The real and imaginary parts of the complex viscosity $\eta^*(\Omega)$ were determined for each experimental run from the phase angle and the amplitude of the film thickness using eqn. (5.18). For many of the visicorder outputs, it was found that the maximum and minimum film thicknesses did not occur at exactly 180° apart. Hence a numerical value for the phase angle was obtained by taking the arithmetic mean of the phase angles measured at the maximum and minimum thicknesses.

The values of $\eta'(\Omega)$ and $\eta''(\Omega)/\Omega$ are plotted against Ω in Fig. 9 for TLA 227 and in Fig. 10 for STP. There is some scatter in the data, but this appears to be random with no apparent dependence upon any parameter other than the angular velocity, which is in agreement with the predictions of section 6 that η^* depends upon the angular velocity alone. The scatter in the data could be attributed to several causes. Chief among these are potential temperature variations between experimental runs, small inaccuracies in the measured values of the phase angles and possible distortion of the true film thickness distribution around the circumference as a consequence of the slight warping which developed along the axis of the Plexiglas cylinder during the course of the experimental program.

A standard procedure for the determination of $\eta^*(\Omega)$ is from torque measurements on an oscillating cone-and-plate viscometer [9]. The values of η' and η'' for the samples of TLA 227 and STP used in the cylinder experiments were determined in this way using a Rheometrics Dynamic Spectrometer, and the resulting data are included in Figs. 9 and 10. The values of $\eta'(\Omega)$ and $\eta''(\Omega)$ obtained from the rimming flow experiments agree well with oscillating cone-and-plate results, particularly considering the possible sources of experimental scatter in the rimming flow data.

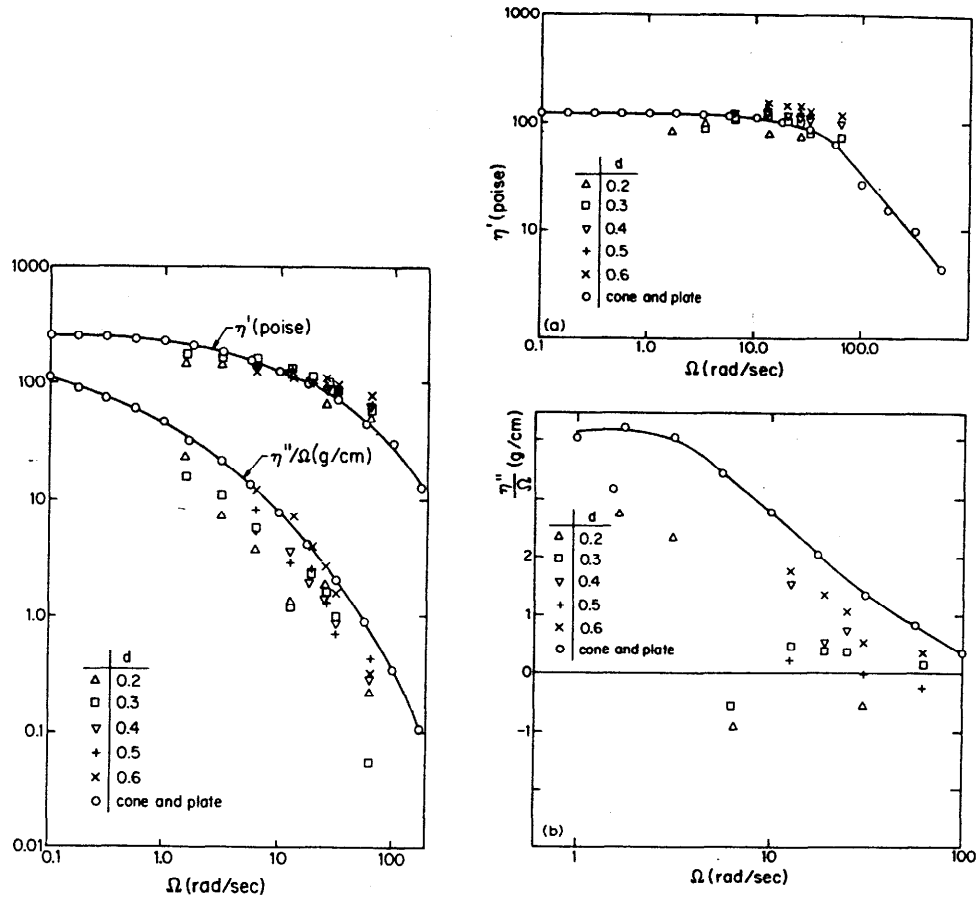

Fig. 9. Viscoelastic data measured for TLA 227.

Fig. 10. Viscoelastic data measured for STP.

It will be noted from Figs. 9 and 10 that the range of angular velocities over which data have been obtained in the rimming flow experiments is limited at both small and large angular velocities. At low angular velocities, the liquid film becomes unstable and degenerates into a number of axially distributed cells. At high angular speeds, the circumferential variation in the film thickness becomes very small, with the result that the output signal is very weak and electronic noise in the output signal becomes significant. It is possible that the high-speed limitation can be improved significantly by more sophisticated electronic filtering and signal-processing devices. A secondary restriction at high speeds with the present experiment was the limited response time of the visicorder used to register the output signals.

The calculations to generate the rheological data in Figs. 9 and 10 were all performed within the linear theory (in ϵ). The perturbation parameter $\epsilon = g/R_0\Omega^2$ (or the parameter $gD^2\rho/3\Omega R_0|\eta^*(\Omega)|$, see section 7.4) gets large for small rotational speed Ω, so that it might be anticipated that the data obtained from the rimming flow experiments would begin to diverge significantly from the cone-and-plate data at low angular speeds. However, the rimming flow results do not appear to differ from the cone-and-plate results at low rotational speeds down to the values at which the film becomes unstable. Thus it would appear that for TLA 227 and STP the higher-order effects are within the range of experimental scatter, and that the film becomes unstable before higher-order effects begin to dominate the flow.

The present experiment represents a first attempt to use a rimming flow experiment to generate information about the complex viscosity $\eta^*(\Omega)$. Although the results of this experiment exhibit some scatter when compared with the corresponding cone-and-plate results, the overall agreement suggests that it may be possible to develop this technique into a potential method for the determination of $\eta^*(\Omega)$.

12.2 Remarks on stability

We conclude with some brief general qualitative observations on the stability of the rimming flow pattern.

The stable circumferential distribution of the liquid film loses its stability as the rotational speed is reduced, and eventually assumes a stable cellular distribution in the axial direction at low enough angular speeds. As the speed is reduced from a value at which the liquid film is stable, the first sign of instability is a two-dimensional out-of-round motion in the r–ϕ plane. The maximum film thickness no longer occurs at a fixed angle, but moves in the direction of the cylinder rotation.

If the speed Ω is reduced further, the out-of-round motion gets stronger and breaks up into regular cell patterns along the cylinder axis. The development of two different cellular patterns is shown in Figs. 11 and 12. For both patterns the cylinder is initially rotating horizontally at a high angular speed. The speed is then reduced rapidly to a value at which cells are known to develop. The only difference between the conditions for Fig. 11 and Fig. 12 is the final rotational speed at which the cells are allowed to develop. The number of cells that develop in the cylinder varies with the amount of liquid in the cylinder and with the rotational speed at which the cells are allowed to form. The flow may be quite irregular while the cells are forming, but once the cells have developed they are very stable provided the rotational speed is not changed very much. This is illustrated in Fig. 12(d) and (e). These two photographs were taken 2 h apart, and yet the cellular patterns appear almost identical.

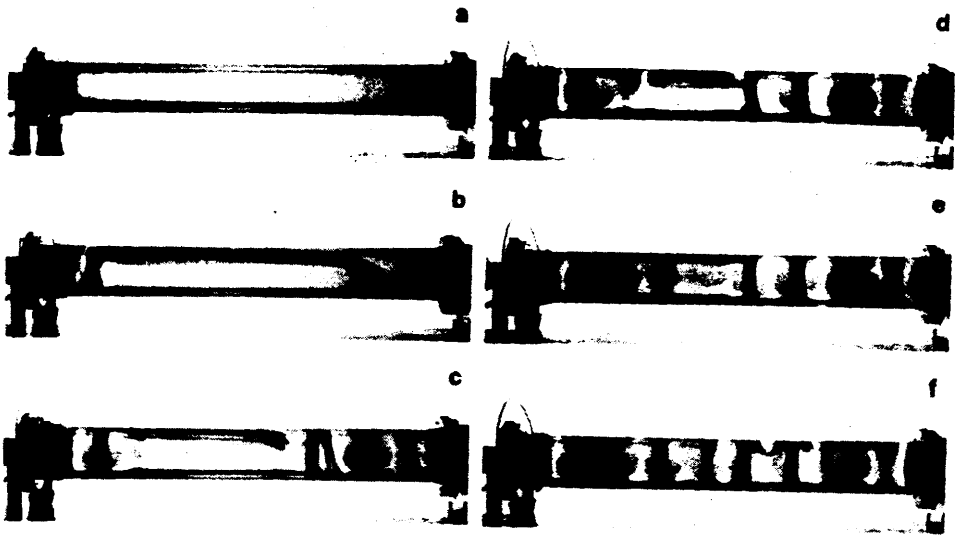

Fig. 11. The development of a cellular configuration from a uniform film thickness configuration. The cylinder is initially rotating at high speed. The speed is suddenly changed to 0.17 rev s^{-1} and held constant at that value. Time (in minutes) from speed change: (a) 0; (b) 1.0; (c) 2.0; (d) 2.5; (e) 3.0; (f) 3.5.

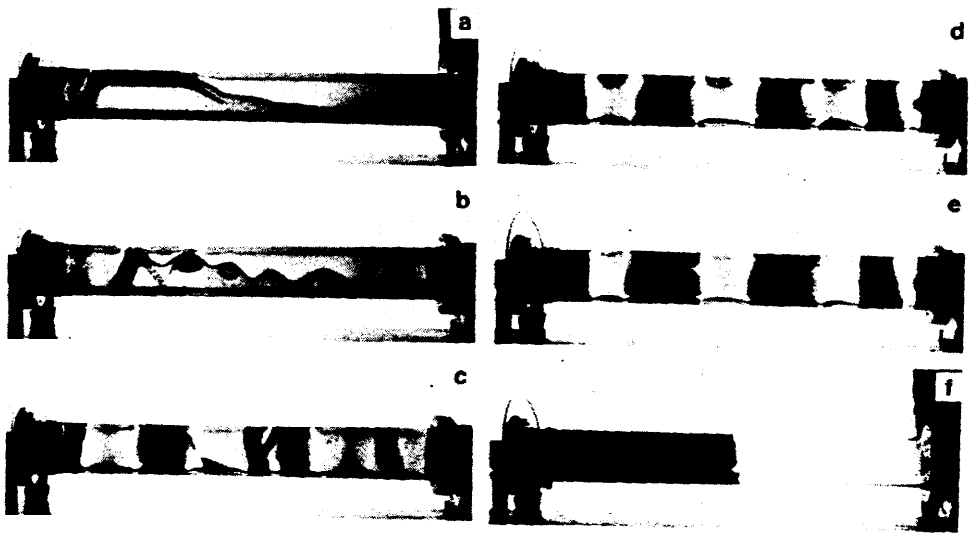

Fig. 12. (a)–(e) The development of a cellular configuration from a uniform film thickness configuration. The cylinder is initially rotating at high speed. The speed is suddenly changed to 0.33 rev s^{-1} and held constant at that value. Time (in minutes) from speed change: (a) 1.5; (b) 3.0; (c) 5.0; (d) 13; (e) 120. The final configuration is stable and unchanging (compare parts (d) and (e)). (f) Single cell formed by rotating cylinder at 0.33 rev s^{-1} in the vertical position and then turning the cylinder to the horizontal position while the cylinder continues to rotate. The liquid stays at the left end of the cylinder provided the rotational speed does not change.

A cellular pattern consisting of a single large cell at one end of the cylinder is shown in Fig. 12(f). This cell was generated by rotating the cylinder slowly in the vertical position and then turning the cylinder into the horizontal position as it continued to rotate. The cell is stable in the horizontal position as long as the cylinder continues to rotate.

The effects described above do not seem to be greatly influenced by the non-Newtonian characteristics of the liquids. Similar behavior was observed with very viscous Newtonian liquids. However, the stability behavior is qualitatively different for low viscosity liquids. Deiber and Cerro [6] describe experimental and numerical results for a wide range of parameters and find two other distinct instability patterns. Phillips [16] describes instability patterns for water waves. Regular cell patterns with water were observed by Karweit and Corrsin [17] who note that cells with water appear only "when the cylinder rotation speed is approached from below". Cells with water are very thin and appear at higher rotational speeds.

Acknowledgements

This work was supported by the U.S. Army Research Office. We gratefully acknowledge the skilful craftsmanship of Mr. Roger Erickson and Mr. William Marquardt throughout the design and construction of the experiment, and the help of Mr. Dirk Sanders and Mr. Austris Cers.

References

1 K.J. Ruschak and L.E. Scriven, Rimming flow of liquid in a rotating horizontal cylinder, J. Fluid Mech., 76(1) (1976) 113–125.
2 B.D. Coleman and W. Noll, Foundations of linear viscoelasticity, Rev. Mod. Phys., 33 (1961) 239–249.
3 D.D. Joseph, Rotating simple fluids, Arch. Rat. Mech. Anal., 66 (1977) 311–344.
4 D.D. Joseph and G.S. Beavers, Free surface problems in rheological fluid mechanics, Rheol. Acta, 16 (1977) 169–189.
5 F.M. Orr and L.E. Scriven, Rimming flow: numerical simulation of steady, viscous, free-surface flow with surface tension, J. Fluid Mech., 84(1) (1978) 145–165.
6 J.A. Deiber and R.L. Cerro, Viscous flow with a free surface inside a horizontal rotating drum. I. Hydrodynamics, Ind. Eng. Chem. Fundam., 15(2) (1976) 102–110.
7 D.D. Joseph, Domain perturbations: the higher order theory of infinitesimal water waves, Arch. Rat. Mech. Anal., 51 (1973) 295–303.
8 K. Walters, Rheometrical flow systems. Part I. Flow between concentric spheres rotating about different axes, J. Fluid Mech., 40 (1970) 191–203.
9 R. Bird, R.C. Armstrong and D. Hassager, Dynamics of Polymeric Liquids, Vol. 1, John Wiley and Sons, New York, 1977.
10 H.K. Moffat, Behaviour of a viscous film on the outer surface of a rotating cylinder, J. Mécanique, 16(5) (1977) 651–673.
11 J. Sanders, Roller coating by viscoelastic liquids, Ph. D. Thesis, University of Minnesota, 1981.

12 G.S. Beavers and D.D. Joseph, Rotating rod viscometer, J. Fluid Mech., 69(3) (1975) 475–511.
13 B.E.D. Kolpin, The oscillating rod viscometer, M. S. Thesis, University of Minnesota, 1977.
14 B.E.D. Kolpin, G.S. Beavers and D.D. Joseph, The free surface on a simple fluid between cylinders undergoing torsional oscillations. Part IV. Oscillating rods, J. Rheol., 24(6) (1980) 719–739.
15 J.Y. Yoo, D.D. Joseph and G.S. Beavers, Higher order theory of the Weissenberg effect, J. Fluid Mech., 92(3) (1979) 529–590.
16 O.M. Phillips, Centrifugal waves, J. Fluid Mech., 7 (1959) 340–352.
17 M.J. Karweit and S. Corrsin, Observation of cellular patterns in a partly filled, horizontal, rotating cylinder, Phys. Fluids, 18(1) (1975) 111–112.